communications earth & environment

ARTICLE

https://doi.org/10.1038/s43247-021-00159-x OPEN

Impacts may provide heat for aqueous alteration and organic solid formation on asteroid parent bodies

Minami Yasui [1✉], Taku Tazawa[1], Ryohei Hashimoto[2], Masahiko Arakawa [1] & Kazunori Ogawa [1,3]

Chemical reactions on asteroid parent bodies, such as aqueous alteration and the formation of organic solids, require a heat source. Radioactive decay in the interiors of these bodies is generally considered the most important heat source, but impact-generated heating is also likely to play a role. Here we present high-velocity impact cratering experiments using thermocouples embedded in the target material to directly measure the spatial and temporal evolution of temperature throughout each impact experiment. We find that the maximum temperature below the crater floor scales with the distance from the impact point, while the duration of temperature rise is scaled by the thermal diffusion time. We use numerical modelling to suggest that, at distances within 2 astronomical units, impacts producing craters of >20 km radius can facilitate aqueous alteration in the material below the crater, while those which produce craters of 1 km radius can support organic solid formation.

[1] Graduate School of Science, Kobe University, Kobe, Japan. [2] Faculty of Science, Kobe University, Kobe, Japan. [3] JAXA Space Exploration Center, Japan Aerospace Exploration Agency, Sagamihara, Japan. ✉email: minami.yasui@pearl.kobe-u.ac.jp

Heat source is one of the main factors controlling the evolution of the parent bodies of asteroids. In the parent body interior, the heat source triggers hydrothermal reactions between water ice and rocks and causes chemical reactions of solutions to create organic solid materials even at 0 °C. For example, many of the carbonaceous chondrites that were delivered from C-type asteroids experienced aqueous processes[1], and their mineralogical analysis showed that their parent bodies had been heated up to 50–150 °C[2]. The heat sources of the parent bodies of carbonaceous chondrites have been debated for more than 50 years. One of the plausible heat sources is radioactive heating of a short-lived radioactive element, ^{26}Al[3]. Aqueous alteration may have occurred in the parent bodies by the heating of ^{26}Al in the early history of the solar system, although the efficiency of ^{26}Al heating might depend on the timing of the accretion of the parent bodies[4].

Another candidate for the heat sources of the parent bodies of asteroids is impact heating[5]. The relative velocity among asteroids in the main asteroid belt is estimated to be 4–5 km s^{-1} [6], so high shock pressure would have been induced by their collision, and the associated shock heat would have raised the temperature around an impact crater instantaneously. These mutual collisions among small bodies are a common phenomenon throughout the history of the solar system, so impact heating is a possible candidate for the heat sources, and could have continued as a heat source even after the radioactive heating by ^{26}Al ceased. Moreover, some asteroids have low bulk density[7]: e.g., the bulk porosity of 253 Mathilde is estimated to be ~50%[8]. Since the shock pressure is rapidly attenuated in such porous bodies[9], a large fraction of the impactor's kinetic energy could be consumed by the plastic deformation accompanied by the crushing out of pores, resulting in effective heating around the impact crater. Impact heating is thus one of the most important heat sources on porous parent bodies. Nonetheless, the effects of impact heating have not been directly studied, although there have been many numerical simulations on the effects of impact heating[10,11].

In this study, we focus on impact heating as a heat source of porous parent bodies and try to measure the temperature around the impact crater directly, in order to investigate the heat generation and dissipation during the impacts. For this purpose, we conducted high-velocity impact experiments of porous gypsum with a porosity of 50%. Our experimental results showed that the temperature distribution caused by post-shock heat and the duration of post-shock heating are scaled by the crater radius and the thermal diffusion time, respectively, and these findings were confirmed by the heat conduction model. Finally, our model showed that the thermal metamorphism caused by post-shock heating could take place on small asteroids.

Results

Temperature change with time. Figure 1 shows the temperature change with time at different distances from the impact point, L_i, for (a) a polycarbonate projectile impacted at 1.7 km s^{-1} and (b) an aluminum projectile impacted at 4.3 km s^{-1}, respectively (see the Methods section). The temperature change, $\triangle T$, is the difference in temperature between before and after the impact. At L_1 in both figures, the $\triangle T$ rose drastically just after the impact and then dropped gradually as the time passed. The $\triangle T$ was very sensitive to the L_i at L_i< 12 mm; for example, the maximum $\triangle T$ at $i = 1$ was more than 5 times larger than that at $i = 2$, while it was less than 1 °C at L_i> 12 mm in both figures.

We analyzed three parameters characterizing the temperature profile as expressed in Fig. 1c: (1) the maximum temperature, $\triangle T_{max}$; (2) the elapsed time at $\triangle T_{max}$, t_{max}; and (3) the half width, $\triangle t_{half}$. We examined the relationship between these parameters and the distance L_i. Since we used two types of projectiles at different impact velocities, we introduced the normalized distance, that is, the distance from the impact point normalized by the transient crater radius, L_i/R_{tr}, to scale the

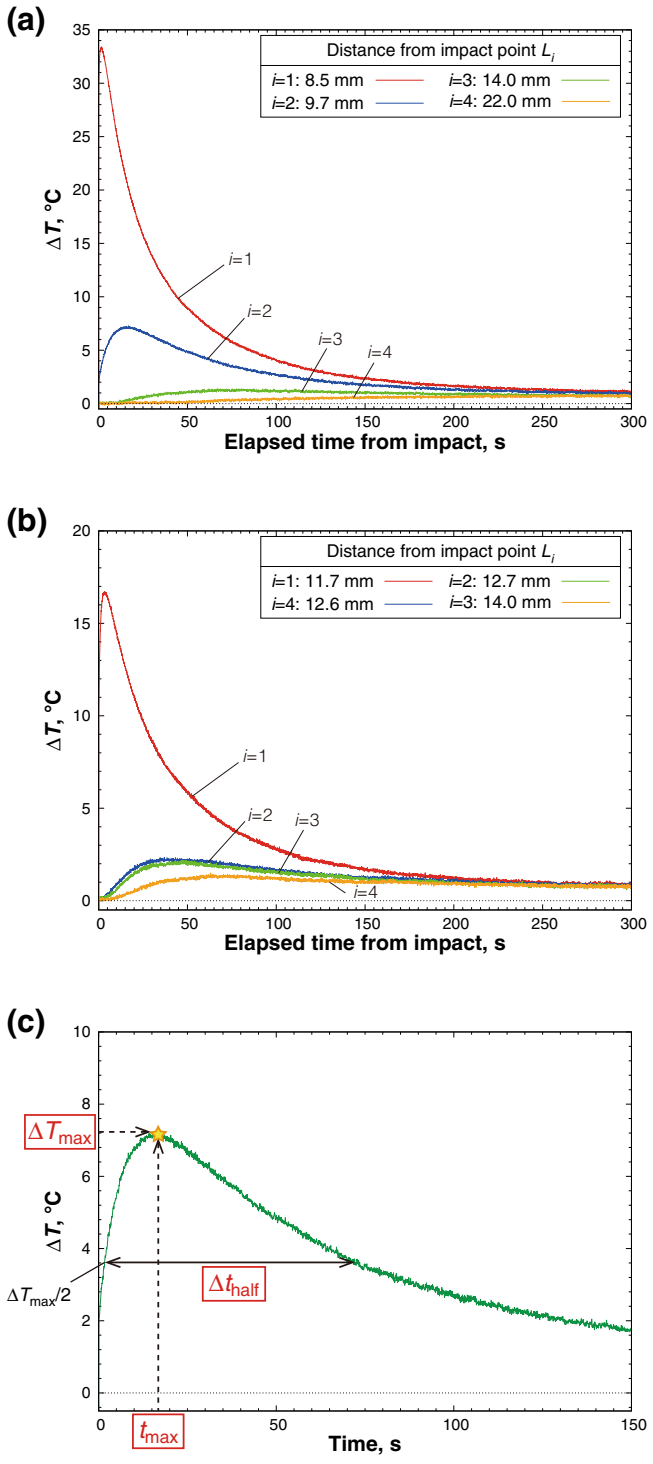

Fig. 1 Temperature change profiles. a Temperature change with time for a polycarbonate projectile at the impact velocity, v_i = 1.73 km s^{-1} (shot number: 180706-1). The $\triangle T$ is the difference from the average temperature before the impact. The time 0 is the impact time. **b** Temperature change with time for an aluminum projectile at v_i = 4.27 km s^{-1} (shot number: 180828-2). **c** Typical temperature change profile. The physical properties of the temperature profile that we measured in this study are shown. Parameters are described in the main text.

degree of impact energy deposited on the target surface. The R_{tr} is defined in Supplementary Method 2, and all results about crater dimensions are summarized in Supplementary Data 1 and Supplementary Figs. 4 and 5. Supplementary Data 2 summarizes the results for each of the three parameters under each impact condition.

Maximum temperature. Figure 2a shows the relationship between the maximum temperature, $\triangle T_{max}$, and the normalized distance, L_i/R_{tr}. Most of the data were consistent within the margin of error, irrespective of projectile types and impact velocity, and the $\triangle T_{max}$ decreased with the increase of the L_i/R_{tr}. The relationship is approximated by the following power law equation:

$$\triangle T_{max} = 10^{2.46 \pm 0.16} \cdot \left(L_i/R_{tr}\right)^{-4.02 \pm 0.34}. \quad (1)$$

The power law index of L_i/R_{tr} in Eq. (1) was −4.0, and this was the decay constant of the $\triangle T_{max}$ with distance around the impact crater on porous gypsum. The $\triangle T_{max}$ at $L_i/R_{tr} = 1$ means the temperature on the crater floor was maximal just after the impact; i.e., it was caused by the heat which was left after the rarefaction wave released the shock compression state. From Eq. (1), the $\triangle T_{max}$ at $L_i/R_{tr} = 1$ was calculated to be 288 °C. In order to confirm this result, we measured the temperature on the crater floor by using a high-speed IR camera as shown in Fig. 2b (for details see Supplementary Method 4), and the $\triangle T_{max}$ was determined to be ~109 °C at 6.7 ms after the impact (Fig. 2c). The crater floor temperature derived from Eq. (1) is higher than that obtained by the IR camera, because the IR camera limit was lower than 183 °C and the measured temperature was over the upper limit at 0 ms; we therefore anticipated that the crater floor temperature cooled rapidly below 129 °C ($\triangle T_{max}$ =109 °C) by thermal radiation within 6.7 ms. Thus, 109 °C is considered to be the lower limit of $\triangle T_{max}$ at L_i/R_{tr} =1.

It is reasonable to assume that the temperature distribution under the crater floor was controlled by only heat conduction after the post-shock heat was deposited in the shell on the crater floor. Since the crater formation was finished within 0.1 ms[12] and the thermal diffusion time of porous gypsum was larger than 10 s, we consider that no heat conduction from the crater floor to the subsurface occurred during the crater formation. Thus, the $\triangle T_{max}$ can be reproduced by the heat conduction model with the initial condition that only the crater floor was heated, and we compared our obtained $\triangle T_{max}$ with the results of numerical simulations for the heat conduction. The heat conduction model is described in detail in Supplementary Method 3, and in Supplementary Fig. 6. The typical results of temperature history at various distances from the impact point are shown in Supplementary Fig. 7, and the parameters used in this calculation are summarized in Supplementary Table 1. In this model, the initial temperature raised by the post-shock heat deposited after the impact, T_{c_ini}, was set to 110 °C in the shell with a thickness of n_{c_ini} on the crater floor, with consideration for the surface temperature of porous gypsum measured by the IR camera at 6.7 ms after the impact. The results of the numerical simulation agreed very well with the experimental results shown in Fig. 2a when the shell thickness was assumed to be 3 mm, which is comparable with the projectile diameter. We calculated the case of the crater with radius $R = 7$ km, six orders of magnitude larger than that in this calculation ($R = \sim 7$ mm) by the same heat conductive model (here, the n_{c_ini}/R was assumed to be constant), and obtained calculated results identical to those shown on the "Model" line on Fig. 2a. Thus, Eq. (1) is applicable for the collisions among parent bodies of asteroids on a larger scale.

According to this model, it is reasonable to estimate the post-shock heat using $E_h = m_s c \triangle T$, where m_s is the mass of the shell with a thickness of 3 mm, c is the specific heat (we assumed to be 1050 J kg^{-1} K^{-1} in this study), and $\triangle T$ =110 °C. The E_h was calculated for shot numbers of 180706-1, 180827-4, and 180622-1 (Supplementary Data 1 and 2), and the ratio of E_h to the projectile kinetic energy was obtained as ~20%.

Timing of the peak temperature and duration. Next, the timing of peak temperature at each L_i is shown in Fig. 3a; the figure shows the relationship between the t_{max} and the L_i/R_{tr}. In Fig. 3a, it is clear that the t_{max} was longer at larger L_i/R_{tr} as the post-shock heat propagated into the target. However, the t_{max} was so scattered at $L_i/R_{tr} > 3$ because only the distance L_i was scaled by the R_{tr}. In order to scale the t_{max}, it is normalized by the thermal diffusion time τ, which is defined as l^2/κ; the l is the thermal diffusion length and it was assumed to be equal to R_{tr}, and the κ is the thermal diffusivity and is calculated as $k/\rho_t c$, where k is the thermal conductivity (0.42 W m^{-1} K^{-1} as measured in this study; see Supplementary Method 1 and Supplementary Fig. 3), ρ_t is the target density (1030 kg m^{-3}), and c is the specific heat (1050 J kg^{-1} K^{-1}). The results are shown in Fig. 3b; the normalized t_{max} was well scaled and it increased with the increase of the L_i/R_{tr}, irrespective of projectile types and impact velocity. The data can be fitted by one quadratic function when $t_{max}/\tau = 0$ at $L_i/R_{tr} = 1$, and the empirical equation was obtained as follows:

$$t_{max}/\tau = (0.14 \pm 0.14) + (-0.30 \pm 0.11) \cdot (L_i/R_{tr}) + (0.16 \pm 0.02) \cdot (L_i/R_{tr})^2. \quad (2)$$

Similarly, the $\triangle t_{half}$ representing the duration of the $\triangle T_{max}$ was scaled by the τ as shown in Fig. 3d, because the $\triangle t_{half}$ was so scattered at $L_i/R_{tr} > 4$, as shown in Fig. 3c. Just as for the t_{max}, the $\triangle t_{half}/\tau$ also increased with the increase of the L_i/R_{tr}, irrespective of the projectile types and impact velocity. Thus, the data can also be fitted by one quadratic function when $\triangle t_{half}/\tau = 0$ at $L_i/R_{tr} = 1$, and the empirical equation was obtained as follows:

$$\triangle t_{half}/\tau = -(0.257 \pm 0.261) + (0.004 \pm 0.215) \cdot (L_i/R_{tr}) + (0.253 \pm 0.045) \cdot (L_i/R_{tr})^2. \quad (3)$$

Discussion

According to the thermal evolution model of parent bodies of asteroids, the surfaces of the parent bodies could be kept low temperature and the ^{26}Al did not heat their surfaces during their evolution[13]. On the other hand, the heat from the impact accompanied with the crater formation would have affected only the surfaces of the parent bodies. Thus, in this study we investigated the thermal metamorphism associated with the crater formation on the surface of the parent bodies of asteroids. First, we discussed the possibility of hydrothermal reactions and organic solid formation in solutions below the crater floor on the parent bodies of asteroids. In this discussion, we adopted the hypothesis that organic solid matters were formed by formose condensation reactions on the parent bodies of asteroids[14], although the organic solid matters could be formed in the interstellar molecular cloud prior to the planetesimal formation[15,16]. We set the critical temperatures necessary for the above processes as follows: aqueous alteration occurs at 50–150 °C[2] and organic solid formation occurs at 0–100 °C[14]. We also consider the time scale of the above processes. The duration of aqueous alteration was reported to be 4 Ma at least in the parent bodies of CM chondrites[17], and that necessary for organic solid formation was reported to be from at least several

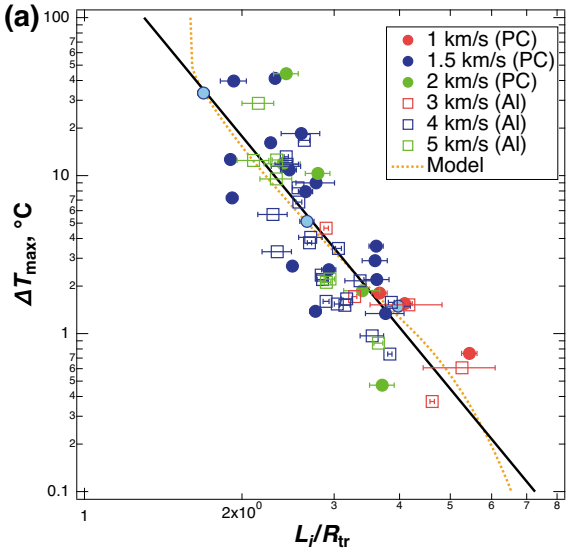

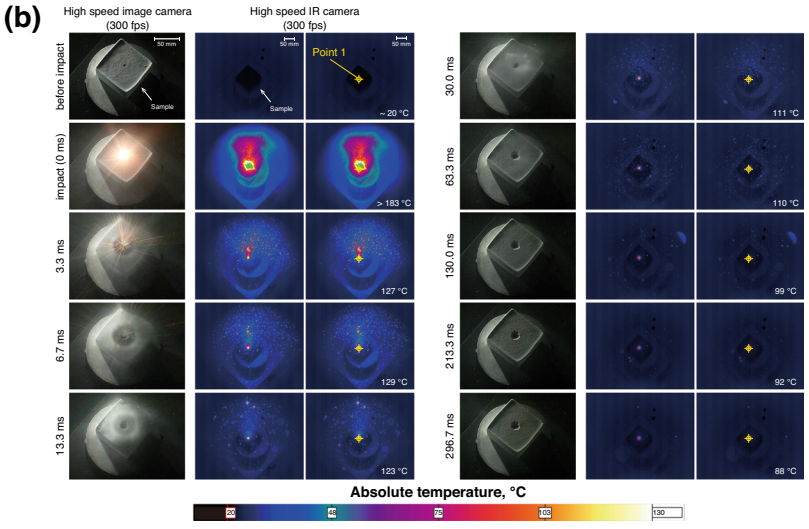

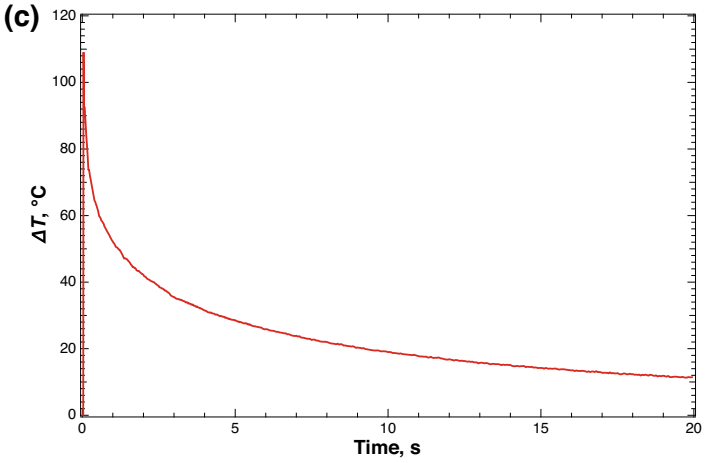

tens of days at 100 °C to at least several tens of kyr at 0 °C[18]. In order to discuss where these processes were realized below the crater floor, we estimated the peak temperature and the duration by using our obtained Eqs. (1) and (3). Here, we calculated the temperature distributions below the crater floor on the parent bodies of asteroids residing at 1.5, 2, and 4 au, and the surface temperature was assumed to be the radiative equilibrium temperature determined by the solar radiation flux (see Supplementary Method 5). Figure 4a shows a cross section of the impact crater with isotherm contour lines at 1.5–4 au. Since the surface

Fig. 2 Maximum temperature and results of the high-speed IR camera imaging. a Relationship between the maximum temperature, $\triangle T_{max}$, and the distance from the impact point normalized by the transient crater radius, L_i/R_{tr}. The black solid line represents the fitting line determined by Eq. (1). The orange dotted line represents the numerical results obtained using a one-dimensional heat conduction model (for details see Supplementary Method 3). PC and Al in the legends stand for the polycarbonate and the aluminum projectiles, respectively. The three light blue circle symbols enclosed with a thick dark blue line show the data compared with the numerical results shown in Supplementary Fig. 7. The error bar on the horizontal axis represents the difference between the maximum radius of the measured transient crater and the average one. **b** Image sequences obtained using the high-speed image camera and high-speed IR camera. The color bar shows the absolute temperature of the images of the IR camera. The number at the left of the first column represents the elapsed time from the impact (0 ms). The temperature in the third column at each time point is the temperature at Point 1. The scale bars are shown on the first images of all columns. **c** Temperature change $\triangle T$ at Point 1 on the third column of **b**. The peak $\triangle T$ at 0 ms might be the lower limit.

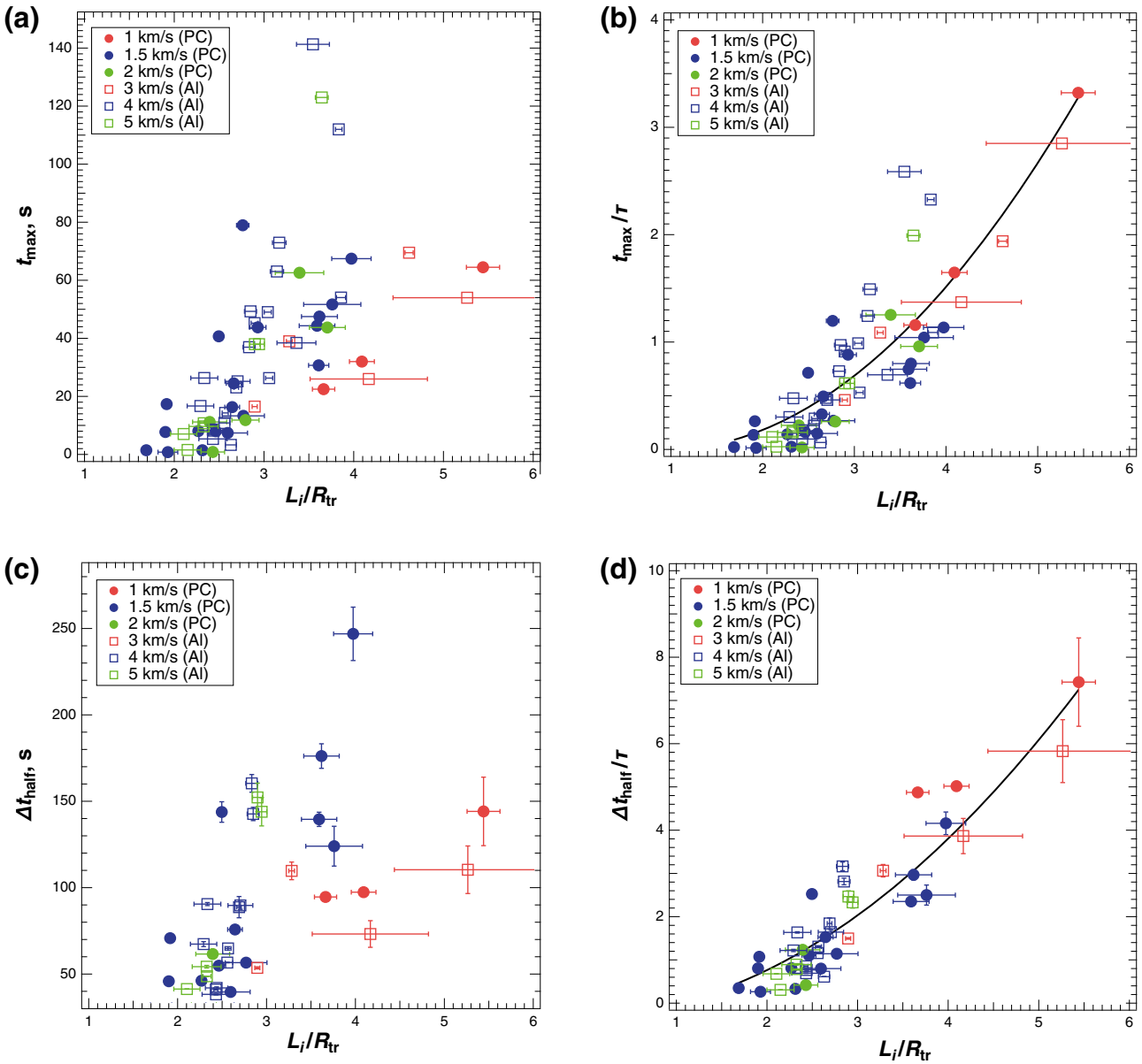

Fig. 3 Timing of the maximum temperature and duration of the temperature rise. a Relationship between the elapsed time at the maximum temperature ($\triangle T_{max}$), t_{max}, and the distance from the impact point normalized by the transient crater radius, L_i/R_{tr}. PC and Al in the legends stand for the polycarbonate and the aluminum projectiles, respectively. **b** Relationship between the t_{max} normalized by the thermal diffusion time, τ, and the normalized distance, L_i/R_{tr}. The solid line represents the fitting line determined by Eq. (2). **c** Relationship between the half width, Δt_{half}, and the normalized distance, L_i/R_{tr}. **d** Relationship between the Δt_{half} normalized by the thermal diffusion time, τ, and the normalized distance, L_i/R_{tr}. The solid line is the the fitting line determined by Eq. (3). The error bar on the horizontal axis in all panels represents the difference between the maximum radius of the measured transient crater and the average one. The error bar on the vertical axis in **c** and **d** represents the duration caused by the temperature fluctuation at the half of the maximum temperature, $\triangle T_{max}/2$.

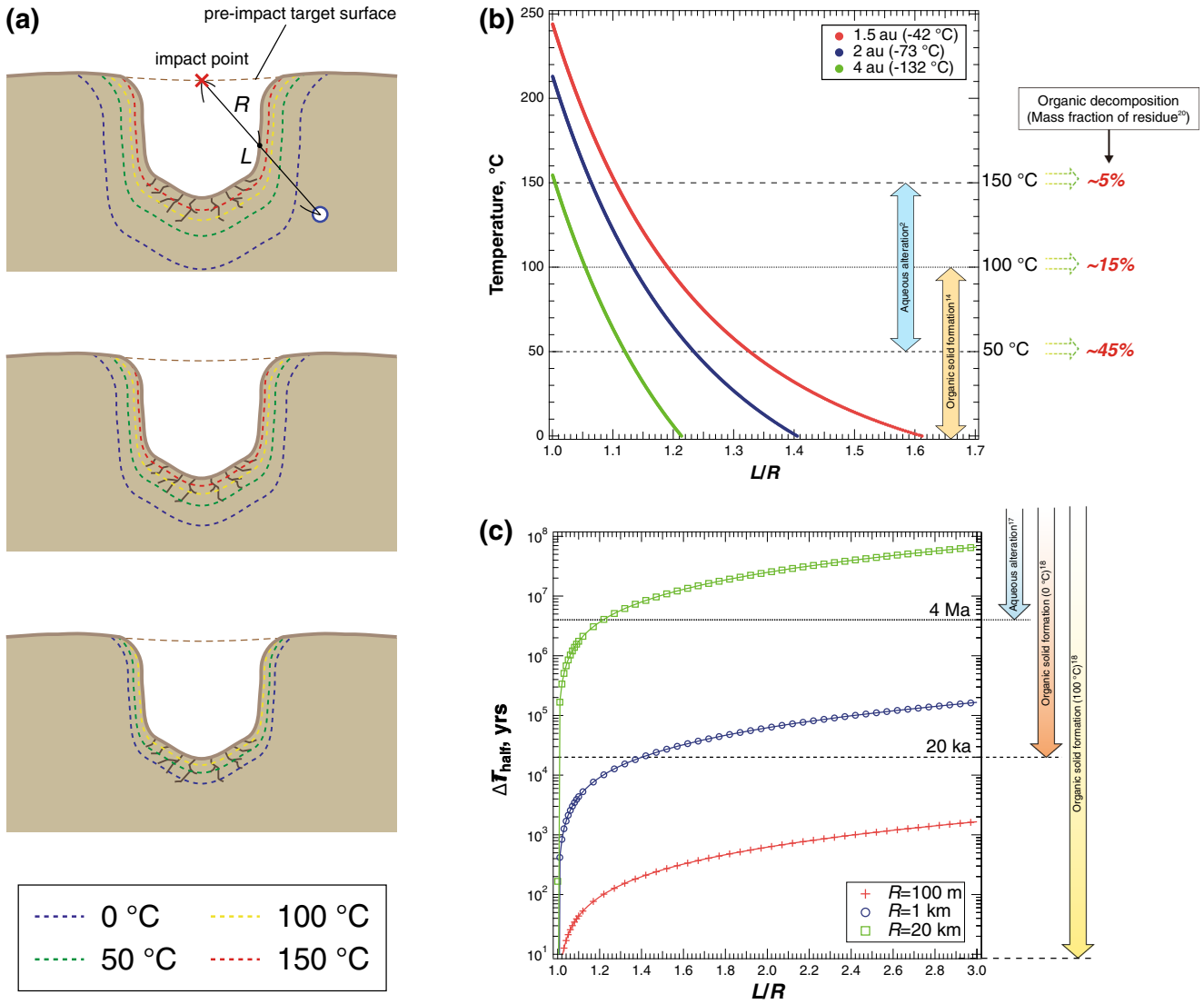

Fig. 4 Thermal metamorphism below the crater floor. a Isotherm contour lines (colored dotted lines) below the crater floor estimated by using Eq. (1) in the case of the radiative equilibrium temperature at 1.5 au (top), 2 au (middle), and 4 au (bottom). The brown dashed line represents the pre-impact target surface. The *R* on the top image is the average crater radius measured from the impact point on the pre-impact target surface. The *L* on the top image is the distance between the measured site (white circle enclosed with a blue line) and the impact point (red ×). **b** Relationship between the maximum temperature and the normalized distance, L/R, at the radiative equilibrium temperatures at 1.5, 2, and 4 au estimated from the Eq. (1). The temperatures in the legend are the radiative equilibrium temperatures at each solar distance. The arrows show the temperature ranges at which the aqueous alteration[2] and the organic solid formation could occur[13]. The numbers on the right of the figure show the mass fraction of residue of organic matters at each temperature obtained by the evaporation experiments[19]. **c** Relationship between the half width, Δt_{half}, and the L/R for impact craters with a radius of 100 m, 1 km, and 20 km as estimated from the Eq. (3). The arrows show the duration when the aqueous alteration and the organic solid formation could occur[16,17].

temperature at 1.5 au was −42 °C, which was the highest temperature among them, the crater wall was raised up more than 200 °C and thus the aqueous alteration could have occurred in the narrow region of $(1.10–1.33)L/R$. Moreover, the organic solid formations could have occurred at relatively wide region of $(1.19–1.61)L/R$. These regions are reduced as the solar distance is increased, as shown on the middle and bottom panels of Fig. 4a. Figure 4b shows quantitatively that the aqueous alteration region reduces to $(1.06–1.23)L/R$ at 2 au and $(1.00–1.12)L/R$ at 4 au. The organic solid formation region also reduces to $(1.13–1.41)L/R$ at 2 au and $(1.05–1.21)L/R$ at 4 au. Although we found the candidate regions for the thermal alteration processes on each parent body, we should compare the duration of the temperature rise with that of these processes. Figure 4c shows that a crater larger than 20 km can maintain the increased temperature for >4 Ma necessary for the aqueous alteration at the distance larger than $1.22L/R$; in addition, the crater >1 km can maintain the increased temperature for 20 ka at $>1.40L/R$ and that at >100 m can maintain the increased temperature for several days at any distances, which is necessary for the organic solid formation at 0 °C and 100 °C, respectively. These calculations demonstrated that aqueous alteration can occur below the crater with $R > 20$ km at 1.5 and 2 au, while organic solid formation at 0 °C can occur below the crater with $R > 1$ km at the same solar distance. The organic solid formation at 100 °C can occur below the crater with > 100 m even at 4 au. However, the region affected by post-shock heating is limited around the crater wall within the thickness of 0.2–0.3 times the crater radius for aqueous alteration, and 0.1–0.2 times and 0.2–0.6

times for the organic solid formations at 0 °C and 100 °C, respectively. At the region more than the crater radius from the crater wall, these thermal metamorphisms could not occur.

At 1.5 au, the average relative impact velocity is estimated to be 10–15 km s^{-1} and this velocity range exceeds that of the impact velocity in our experiments[19]. However, the relative impact velocity among parent bodies of asteroids, that is, planetesimals, had a velocity distribution such that some planetesimals at 1.5 au might collide at a relative impact velocity smaller than 5 km s^{-1}. Furthermore, if the energy partition ratio of ~20% (that is, the ratio of the post-shock heat, E_h, to the impactor's kinetic energy) does not change even at >5 km s^{-1}, our obtained empirical equations of Eqs. (1) and (3) could be applicable to the cases of planetesimal collisions at 1.5 au.

On the other hand, the organic matters formed in the interstellar molecular cloud prior to the planetesimal formation could be decomposed due to the post-shock heating that accompanied the crater formation[15,16]. Evaporation experiments were performed on interstellar organic analogs to examine the temperature dependence of the weight loss of the analogs[20]. The results of these experiments are also shown in Fig. 4b. For example, if the temperature around the impact crater rises above 100 °C, the interstellar organic matters could be reduced to 15% of the original mass. Therefore, both synthesis and decomposition of organic solid matter by post-shock heating can occur simultaneously on the parent bodies of asteroids.

Methods

Target samples. We used a porous gypsum block as a target simulating porous asteroids, since porous gypsum was previously used as an analog for small satellites and primitive porous planetesimals[12,21–23]. The porous gypsum target was prepared as follows. The powdered $CaSO_4{\cdot}1/2H_2O$ was mixed with tap water, and then the mixed slurry was put into a rectangular mold. The slurry in the mold was dried in an oven at 55 °C for 4 days in order to completely evaporate water from the inside of the target, and then the porous gypsum was removed from the mold, cut with a bandsaw, and sanded with sandpaper into the desired form. The target had a rectangular shape of 70 mm × 70 mm × 40 mm, as shown in Supplementary Fig. 1a. The target bulk density, ρ_t, was 1.03 (±0.02) g cm^{-3}, corresponding to a porosity of 53 (±1)%.

In order to measure the temperature changes at different sites in the target, a CA (chromel–alumel) thermocouple with a diameter of 127 μm was used. Four or five thermocouples were set in the target by one of two methods. In the first method, the thermocouples were set on the surface of a polished porous gypsum plate of 70 mm × 70 mm × 30 mm, and then another plate of 70 mm × 70 mm × 10 mm was placed atop the first plate and the mixed slurry was poured into the gap between the two plates. In the second method, two very thin nylon strings on which the thermocouples were pinned were set diagonally across the rectangular mold on the dotted black lines shown in Supplementary Fig. 1b, and then the mixed slurry was poured into the mold. After removing the target from the mold, the nylon strings could not be removed from the target. The choice of the method used to set the thermocouples did not affect the experimental results very much. The thermocouples were set at a constant depth from the impact surface (L_y ~10 mm), and at different distances from the centerline normal to the impact surface passing through the impact point: The values of L_x varied widely (Supplementary Fig. 1b). Actually, the distance of the thermocouple from the impact point, L (Supplementary Fig. 1a), was measured for the recovered target after cutting the target surface carefully. One of the examples is shown in Supplementary Fig. 1c–f. By using the top image of the target (Supplementary Fig. 1c) and the crater profiles measured along two directions crossed at right angles (Supplementary Fig. 1d–f), the distance of a thermocouple from the impact point was calculated as $L_i(=\sqrt{{L_{xi}}^2+{L_{yi}}^2})$, where i is the number of a thermocouple in the same shot. In this study, the L was changed from 17.8 to 8.5 mm. The temperatures measured by the thermocouples were recorded by a data logger with an A/D conversion rate of 10 kHz and a resolution of temperature of 0.1 K (Data Platform GL7000; Graphtec, Yokohama, Japan). The impact point was determined by means of the method described in the next section.

Impact experiments. Impact experiments were conducted by using the two-stage horizontal gas gun located at Kobe University. Supplementary Fig. 2a is a schematic illustration of the experimental setup. We used two kinds of projectile: a polycarbonate sphere with a diameter of 4.75 mm, a mass of 68 mg, and a density of 1.2 g cm^{-3} and an aluminum sphere with a diameter of 2 mm, a mass of 12 mg, and a density of 2.7 g cm^{-3}. The projectile was launched in the direction normal to the gravity acceleration of the Earth, and it impacted at a direction normal to the target surface. The impact velocity, v_i, ranged from 5.0 to 1.1 km s^{-1} and most of polycarbonate and aluminum projectiles were accelerated at 1.7–2.0 km s^{-1} and 4.3–5.0 km s^{-1}, respectively.

We observed the impact phenomena by using a high-speed digital video camera (Phantom v1612; Nobby Tech., Tokyo) to confirm that the projectile was separated from the sabot successfully. The frame rate and the exposure time were set at 10^5 frames s^{-1} and 380 ns, respectively. Supplementary Fig. 2b shows the snapshots before and after the impact taken by the high-speed camera. At 0.04–0.02 ms before the impact (the uppermost right image in the first line and the uppermost left one in the second line), the projectile was only appeared in the front of the target, indicating that the sabot separation was succeeded.

The vacuum chamber was evacuated below 25 Pa before each shot. The porous gypsum target was set in the vacuum chamber. The ambient temperature in the vacuum chamber was about 20 °C. Two metal halide lamps were used to illuminate the target to observe the impact phenomena by using the high-speed camera. The temperature of the target surface rose slightly due to the illumination of the metal halide lamps, so we turned the lamps off just after the impact to prevent the temperature rise.

After the shot, we recovered the porous gypsum target and measured two kinds of crater diameter (the diameters of the transient crater and spalling area; these are explained in detail in Supplementary Method 2) by using a digital caliper in four directions. Additionally, the profile of the impact crater was measured by using a laser profiler (#LK-G150; Keyence, Osaka, Japan) to determine the depth of the impact crater.

The impact point was determined by using a photo taken just above the target surface and a profile of the impact crater, because it was difficult to determine the impact point using the high-speed camera images themselves, as shown in the center image in the second line on Supplementary Fig. 2b. The impact surface was assumed to be a plane, as extrapolated by the outer edge of the impact crater profile. The impact point was defined to be the center of the transient crater on the photo taken just above the target, when the transient crater was assumed to be a perfect circle on the photo.

Data availability

The majority of data in this study are included in this published article and its supplementary information files. Other data that support the findings of this study are available at https://doi.org/10.5281/zenodo.4626228.

Code availability

The numerical code is available upon reasonable request. Requests can be made to M.Y. (https://www.minami.yasui@pearl.kobe-u.ac.jp).

Received: 5 October 2020; Accepted: 24 March 2021;
Published online: 18 May 2021

References

1. McSween, H. Y. Jr. Aqueous alteration in in carbonaceous chondrites: mass balance constraints on matrix mineralogy. *Geochim. Cosmochim. Acta* **51**, 2469–2477 (1987).
2. Zolensky, M. E., Bourcier, W. L. & Gooding, J. L. Aqueous alteration on the hydrous asteroids: Results of EQ3/6 computer simulations. *Icarus* **78**, 411–425 (1989).
3. Urey, H. C. The cosmic abundances of potassium, uranium, and thorium and the heat balance of the Earth, the Moon, and Mars. *Proc. Nat. Acad. Sci. USA* **41**, 127–144 (1955).
4. McSween, H. Y. Jr., Ghosh, A., Grimm, R. E., Wilson, L. & Young, E. D. in *Asteroids III* (eds. Bottke, W. et al.) 559–571 (University Arizona Press, 2002).
5. Rubin, A. E. What heated the asteroids? *Sci. Am.* **292**, 80–87 (2005).
6. Bottke, W. F. Jr., Nolan, M. C., Greenberg, R. & Kolvoord, R. A. Velocity distributions among colliding asteroids. *Icarus* **107**, 255–268 (1994).
7. Consolmagno, G. J. & Britt, D. T. The density and porosity of meteorites from the Vatican collection. *Meteorit. Planet Sci.* **33**, 1231–1241 (1998).
8. Britt, D. T., Yeoman, D., Housen, K. & Consolmagno, G. in *Asteroids III* (eds. Bottke, W. et al.) 485–500 (University Arizona Press, 2002).
9. Housen, K. R. & Holsapple, K. A. Impact cratering on porous asteroids. *Icarus* **163**, 102–119 (2003).
10. Davison, T. M., Ciesla, F. J. & Collins, G. S. Post-impact thermal evolution of porous planetesimals. *Geochim. Cosmochim. Acta* **95**, 252–269 (2012).
11. Bland, P. A. et al. Pressure-temperature evolution of primordial solar system solids during impact-induced compaction. *Nat. Commun.* **5**, 5451 (2014).
12. Yasui, M., Arakawa, M., Hasegawa, S., Fujita, F. & Kadono, T. In situ flash X-ray observation of projectile penetration processes and crater cavity growth in porous gypsum target analogous to low-density asteroids. *Icarus* **221**, 646–657 (2012).

13. Castillo-Rogez, J. C. & Schmidt, B. E. Geophysical evolution of the Themis family parent body. *Geophys. Res. Lett.* **37**, L10202 (2010).
14. Kebukawa, Y. & Cody, G. D. A kinetic study of the formation of organic solids from formaldehyde: implications for the origin of extraterrestrial organic solids in primitive solar system objects. *Icarus* **248**, 412–423 (2015).
15. Greenberg, J. M. et al. Approaching the interstellar grain organic refractory component. *Astrophys. J.* **455**, L177–L180 (1995).
16. Herbst, E. & van Dishoeck, E. F. In *Annual Review of Astronomy and Astrophysics* (eds. Blandford, R. et al.) 427–480 (Annual Reviews (US), 2009).
17. de Leuw, S., Rubin, A. E., Schmitt, A. K. & Wasson, J. T. ^{53}Mn–^{53}Cr systematics of carbonates in CM chondrites: implications for the timing and duration of aqueous alteration. *Geochim. Cosmochim. Acta* **73**, 7433–7442 (2009).
18. Briani, G. et al. Short duration thermal metamorphism in CR chondrites. *Geochim. Cosmochim. Acta* **122**, 267–279 (2013).
19. Bottke, W. F. Jr., Nolan, M. C. & Greenberg, R. Collision lifetimes and impact statistics of Near-Earth Asteroids. *LPSC* **24**, 159–160 (1993)
20. Nakano, H., Kouchi, A., Tachibana, S. & Tsuchiyama, A. Evaporation of interstellar organic materials in the solar nebula. *Astrophys. J.* **592**, 1252–1262 (2003).
21. Nakamura, A. M. Impact cratering on porous targets in the strength regime. *Planet. Space Sci.* **149**, 5–13 (2017).
22. Kawakami, S. et al. An experimental study of impact fracturing of small planetary bodies in the solar system with an application to Phobos. *Astron. Astrophys.* **241**, 233–242 (1991).
23. Nakamura, A. M., Yamane, F., Okamoto, T. & Takasawa, S. Size dependence of the disruption threshold: laboratory examination of millimeter–centimeter porous targets. *Planet. Space Sci.* **107**, 45–52 (2015).

Acknowledgements

This study was partly supported by the Hypervelocity Impact Facility, ISAS, JAXA. This study was supported by Grants-in-Aid from the Japan Society for the Promotion of Science (nos. 16H04041, 16K17794, and 19H00719) and the Sumitomo Foundation (no. 150341).

Author contributions

M.Y. designed the experimental setup, analyzed the data, performed the numerical simulation, and cowrote the manuscript and wrote the figures. T.T. and R.H. performed the experiments. M.A. designed the study and the experimental system, and cowrote the manuscript. K.O. constructed the numerical model. All the authors discussed and contributed intellectually to the interpretation of the results.

Competing interests

The authors declare no competing interests.

Additional information

Supplementary information The online version contains supplementary material available at https://doi.org/10.1038/s43247-021-00159-x.

Correspondence and requests for materials should be addressed to M.Y.

Peer review information Primary handling editor: Joe Aslin.

Reprints and permission information is available at http://www.nature.com/reprints

Publisher's note Springer Nature remains neutral with regard to jurisdictional claims in published maps and institutional affiliations.